Virtual asphalt to predict roads' air voids and hydraulic conductivity

M. Aboufoul [a], A. Chiarelli [b], I. Triguero [c], A. Garcia [a*].

[a] *Nottingham Transportation Engineering Centre [NTEC], Department of Civil Engineering, University of Nottingham, Nottingham NG7 2RD, UK*

[b] *Research Consulting Limited, The Ingenuity Centre, University of Nottingham Innovation Park, Triumph Road, Nottingham, NG7 2TU, UK*

[c] *The Automated Scheduling Optimisation and Planning Research Group, School of Computer Science, University of Nottingham, Nottingham, NG8 1BB, U.K*

** Corresponding author. Tel: +44 (0) 0115 95 13914. E-mail addresses: alvaro.garcia@nottingham.ac.uk*

Abstract

This paper investigates the effects of air void topology on hydraulic conductivity in asphalt mixtures with porosity in the range 14%-31%. Virtual asphalt pore networks were generated using the Intersected Stacked Air voids (ISA) method, with its parameters being automatically adjusted by the means of a differential evolution optimisation algorithm, and then 3D printed using transparent resin. Permeability tests were conducted on the resin samples to understand the effects of pore topology on hydraulic conductivity. Moreover, the pore networks generated virtually were compared to real asphalt pore networks captured via X-ray Computed Tomography (CT) scans. The optimised ISA method was able to generate realistic 3D pore networks corresponding to those seen in asphalt mixtures in term of visual, topological, statistical and air void shape properties. It was found that, in the range of porous asphalt materials investigated in this research, the high dispersion in hydraulic conductivity at constant air void content is a function of the average air void diameter. Finally, the relationship between average void diameter and the maximum aggregate size and gradation in porous asphalt materials was investigated.

Keywords: Computational design; optimisation; porosity; pore networks; X-ray CT; 3D printing.

1 INTRODUCTION

Asphalt pavements with porosity ranging between 15% and 26% have complex pore networks that can easily drain water [1]. Thus, porous asphalt is often used to reduce runoff water quantity and improve highway safety [2]. The internal pore structure of porous asphalt is exposed to water for long periods due to its high permeability [3], and moisture damage may happen and negatively affect the bond between the aggregate and binder surface. Typical effects of such phenomena include stripping, cracking and excessive permanent deformation [4]. Therefore, to build durable porous asphalt pavements, water flow and the associated topological factors need to be accurately investigated.

Previous research [1, 5, 6] applied X-ray Computed Tomography (CT) scans to study the effect of the topological properties of the pore space on the hydraulic conductivity of porous materials. However, X-ray CT scans are often expensive and time-consuming. To address the issues of cost and time required, computational methods were developed in the recent years that build pore networks similar to those seen in real porous materials [7]. A range of approaches are available to computationally study granular material pores, including the discrete elements methods (DEM) [8, 9], statistical [10] and mathematical methods [11, 12]. These methods are complex to implement without using commercial software [13] or having a deep background in mathematical modelling.

The Intersected Stacked Air voids (ISA) method is a newly-developed approach to generate virtual pore networks in granular and asphalt materials [7, 14]. The technique was developed based only on geometrical, rather than on physical, principles. The ISA method was created by setting a number of ad-hoc, geometrical, parameters to recreate a specific asphalt mixture, which are described in section 2.4. This typically requires a time consuming manual tuning of those parameters, which makes the use of ISA method to generate realistic pore network not completely efficient. Optimisation techniques [15] are required for ISA methods to obtain best result. Among other alternatives, one can employ a Differential evolution (DE) algorithm [16], which is an evolutionary-based optimisation technique capable of dealing with continuous optimisation. In this study, ISA approach is generalised by the means of DE algorithm that manipulate the ISA input parameters to generate virtual asphalt pores as required by the user, without a time consuming trial-and-error process.

In addition, thanks to the ability to create complex geometric volumes [17-20], 3D printing has recently become an important technique in the fields of flow and transport in porous media. Particularly, Head and Vanorio [21] and Ishutov et al. [22] reported the use of 3D printing to reproduce the complex pore spaces seen in rocks. The use of 3D printing provided a unique opportunity to combine the ISA method – a computational approach – with physical testing on resin samples similar to real asphalt networks.

This study compares the results of physical tests on real and computationally-generated asphalt pore networks to further understand the effects of topological properties such as average void dimeter and Euler number on the hydraulic conductivity of porous asphalt mixture.

2 MATERIALS AND METHODOLOGY

2.1 Porous asphalt samples description

A total of 15 cylindrical porous asphalt samples with 100 mm in diameter and 50 mm in height were manufactured with bitumen 60/40 penetration grade and crushed limestone aggregates. The specimens were prepared with different gradations and three different maximum aggregate sizes (6, 10 and 14 mm). These mixtures aimed to represent porous asphaltic materials commonly used in roads, with different maximum aggregate sizes and porosities (see Table 4 in appendix for the aggregate gradation and binder content used in the mixtures). Aggregates and bitumen were mixed at 160 °C and gyratory-compacted at 140 °C to reach the target porosity of 13%, 17%, 21%, 26% and 29%, following the standard BS EN 12697-31[23].

2.2 X-ray Computed Tomography (CT) scans of asphalt mixture

Asphalt cores were scanned under dry condition using a Phoenix v|tome|x L 300 micro CT scanner; the X-ray tube used is (MXR320HP/11, 3.0mm Be +2mm Al from GE Sensing and Inspection Technology) and was operated with an acceleration voltage of 290 kV and a current of 1300 µA.

The X-ray CT scans were carried out in the micro computed tomography Hounsfield facility at the University of Nottingham. The reconstruction of scans was performed on GE Datos|x reconstruction software with 2x resolution to obtain a spatial resolution of 45.2 µm. The reconstructed X-ray CT scans were used to generate 3D asphalt pore models of different porosity using Avizo 8.1 and ImageJ software. A more detailed overview of the test setup and data interpretation can be found in reference [1].

2.3 3D Printing material and technology

Stereolithography (SLA) printing was used to fabricate the samples due to the technology's ability to produce fine channels and pores with high resolution (25 to 100 µm)[22]. Common materials used in SLA are acrylic clear or translucent resins that contain photo-initiators [24]. When the resin is irradiated with a laser of a wavelength that matches its photo-initiator, a rapid solidification occurs in the form of photo-polymerisation. The 3D printing process is carried out by scanning the surface of the resin with a laser beam to match the required shape layer by layer to form a complete 3D structure [18]. The printed structure was then submerged in isopropanol alcohol (IPA) for 10 minutes to make sure all resin within the pores had come out. Moreover, samples made with SLA printing materials can be considered as

hydrophobic as their mean wetting angle 68.7°±7.67 [25]. This shows that the printing materials used in SLA technology can reproduce asphalt mixture structures with close wetting properties to the real ones, as the mean wetting angle of bitumen 60/40 penetration grade is 93.04°[26]. The wetting angle of mastic is between these two values, which is in the range of SLA printing materials.

2.4 Computational generation of the 3D air pore structures in asphalt material

2.4.1 The porous media generator

In this paper, we propose the use of the ISA method [7, 14, 27] to generate virtual porous networks similar to those seen in real asphalt samples for the purpose of 3D printing. Although the ISA method has been validated numerically in [27] against a limited sample of real asphalt cores, it has not been validated experimentally to date.

The ISA method is a touch-and-stop packing algorithm where small 2D particles (circles or ellipses) are generated in random, non-overlapping positions within a specified subset of $\mathbb{R}^2$ (e.g. a rectangle or a circle). Subsequently, the radius of said particles is increased until all touch either another particle of the edge of the chosen domain. After this first generation of particles has fully grown, new ones can follow, with the condition that their centres of growth are not within any other existing particle (i.e. a form of rejection sampling is employed).

A chosen number of packed domains can be created, and the particles in each plane can be converted to solids, i.e. spheres or ellipsoids. Planes of 3D packed particles can then be layered at a chosen distance from one another, in such a way that particles from different planes are made to intersect.

Finally, the “empty” space left between the layers of packed and intersecting 3D particles can be located by (i) creating a 3D grid of points with a chosen resolution and (ii) computationally checking which points in the grid are not inside any existing particle. The points in the location grid are used to create a 3D Boolean matrix consisting of zeros in the void space and ones in the matter (aggregate/mastic) space.

While the approach used by the ISA method is purely geometrical and, to some extent, arbitrary, its meaningfulness arises from the fact that the sampled void space has properties that are very similar to those of asphalt samples. A sample result of the ISA method can be seen in Figure 1, where the porous space corresponding to an AVC of 19.8 % is shown.

For more details on the process and for a detailed analysis of its steps, we invite readers to consult [14, 27].

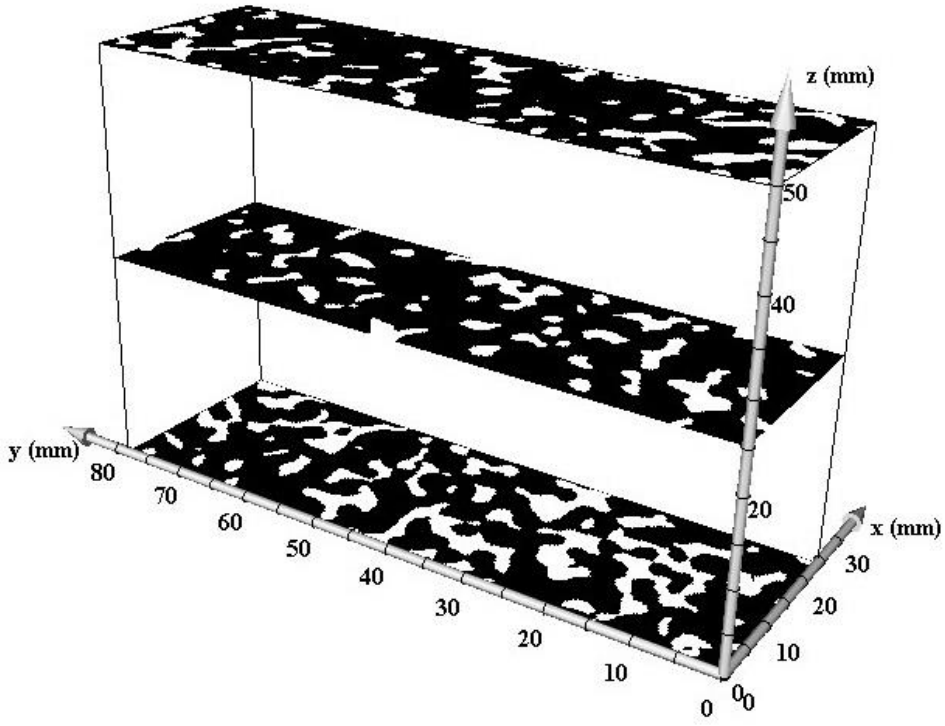

Figure 1: Sample layers result from the ISA methods reproducing an asphalt mixture with 19.8% air void content.

2.4.2 Air voids properties considered

The macropore characteristics considered in this study included macroporosity, average void diameter, Euler number and tortuosity. These properties are commonly used to analyze the topology of soils and porous media [5]. The macroporosity was calculated in MATLAB as the volume of macropores per unit of volume in the region of interest (ROI), while the average void diameter was calculated in MATLAB [28] using a watershed segmentation algorithm to detect and separate pores.

The connectivity of pore networks is commonly expressed based on the Euler number (χ). This was determined from 3D binary images using MATLAB [29]. The macropores tortuosity factor from tomographic X-ray data was calculated using an open source application written in MATLAB (TORT3D) [30].

2.4.3 Optimisation of the packing parameters via Differential Evolution (DE) methods

The main inputs for the ISA algorithm are the number of starting 2D particles, target planar void ratio, starting radius, maximum radius and, distance between packed domains, see Table 1. When the investigator introduces these inputs into the ISA algorithm, the output is an air void structure, which properties can be quantified. The limitation of the ISA algorithm is that the number of input combinations to produce a certain air void structure is too big to be investigated by trial-and-error. For

that reason, a DE algorithm has been used to iterate and optimise the selection of inputs for the ISA method algorithm. DE has shown to perform well in a wide variety of optimisation problem [31], in which the values to be optimised are real values. Furthermore, to limit the computational time and prevent the generation of inconsistent solutions, ranges of the inputs were selected based on the investigators' experience and, the parameters were also rounded to the factors defined in Table 1.

To start the DE algorithm a population of several initial individuals (i.e. solutions to the problem) of input parameters are randomly selected from the allowed ranges [16]; this stage is called initialization. After this, a cycle of mutation and crossover of existing solutions is performed, in which new solutions are created, so that, a fitness value is minimised (or maximise). The first individual is selected and we call it target (red individual in Figure 2); in addition, a number of individuals (usually three) are randomly selected and combined by weighting the differences of two randomly selected individuals (blue vectors in Figure 2) using a scaling factor F and adding the weighted differences to the third one (yellow vector in Figure 2), to produce a mutant individual; this stage is called mutation. Then, a child individual (see Figure 2) is produced by mixing parameters of the mutant and target individuals and, the probability that the child individual inherits parameters from one or the other parent individual is fixed by a crossover constant, which is defined between 0 and 1; this process is called crossover [32].

Finally, we must check which of the child or target individuals will produce better results and select the best one for the next iteration. These stages are repeated in subsequent DE iterations, and a graphic of error versus number of iterations can be produced. In this paper, the error is the difference between the required air void structure and the air void structure generated by the ISA algorithm. The DE algorithm will keep iterating until the error reaches a minimum level or another termination criteria is reached [33], such as a maximum number of iterations. In the literature, this mutation strategy is known as "DE/Rand/1" [31, 34].

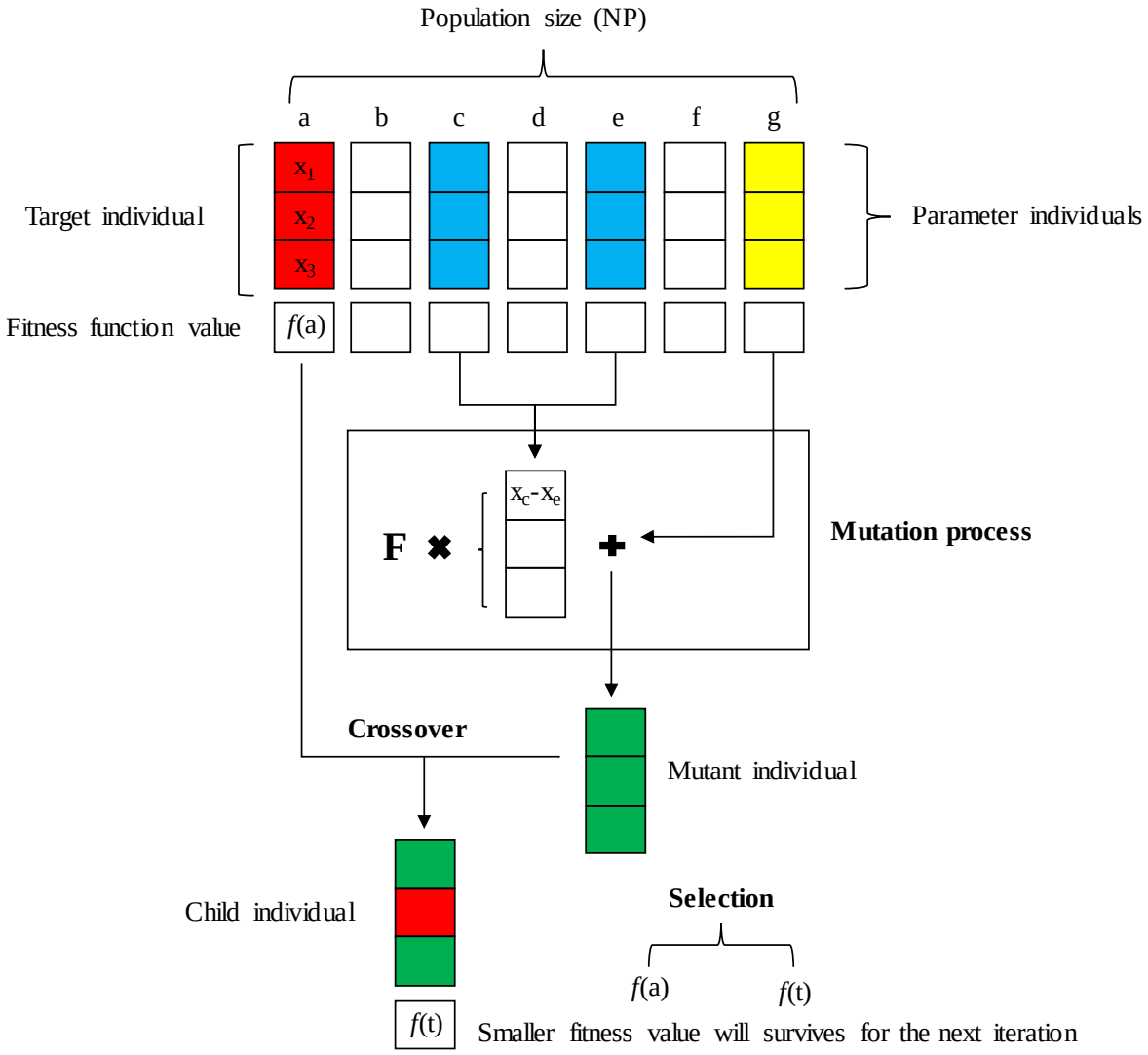

Figure 2: Working of Differential Evolution algorithm

In this paper, the initial number of vectors selected is 10 and, the crossover probability is 0.7, the weighting scaling factor is 0.8 and the maximum number of iterations for the algorithm has been limited to 100. These values have been selected based on experience. The error (E) was defined as:

$$\boldsymbol{E} = (|\boldsymbol{M_R} - \boldsymbol{M_{OUT}}|) + (|\boldsymbol{Avd_R} - \boldsymbol{Avd_{OUT}}|) + (|\boldsymbol{\chi_R} - \boldsymbol{\chi_{OUT}}|) + (|\boldsymbol{T_R} - \boldsymbol{T_{OUT}}|) \quad (1)$$

Where M_R is the required Macroporosity (%) and M_{OUT} is the calcuated Macroporosity (%), Avd_R is the average void diameter (mm), Avd_{OUT} is the calculated air void diameter (mm), χ_R is the required Euler number, χ_{OUT} is the calculated Euler number, T_R is the required tortuosity and T_{OUT} is the calculated tortuosity.

Table 1: Parameters for the DE optimisation algorithm.

Parameter	Unit	Range	Rounding
Number of starting 2D particles	-	70-120	5, e.g. 70, 75, etc.
Target planar void ratio	%	53-63	5, e.g. 58, 62, etc.
Starting radius	mm	0.01-0.1	0.05
Maximum radius	mm	3.7-7.2	0.5
Distance between packed domains	-	0.8-0.95	0.05

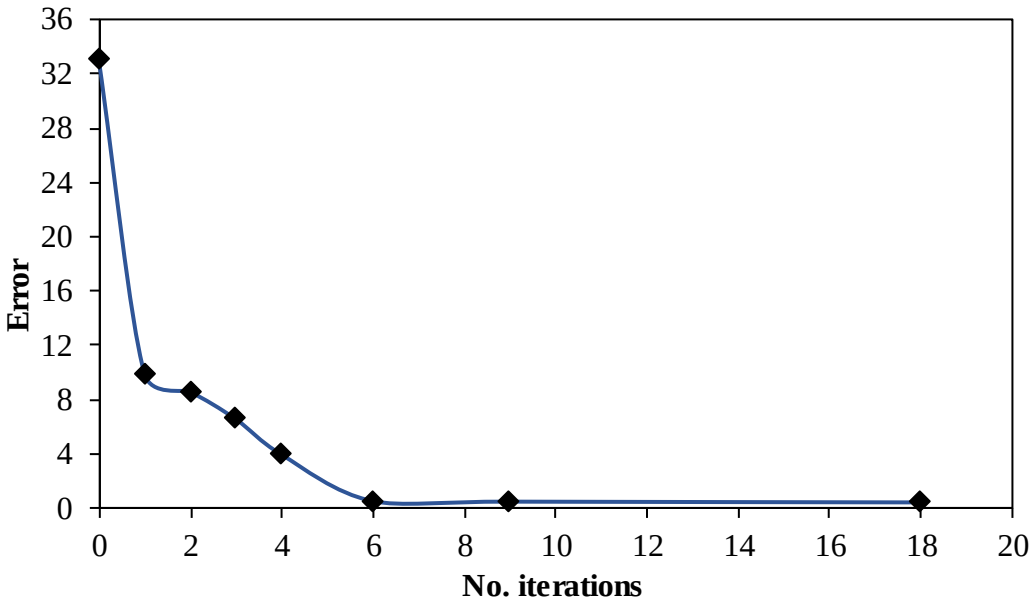

Figure 3: Error versus number of iterations.

2.5 3D printed test samples generation

Six sets of 3D printed samples were fabricated (see Table 2). First, set 1 consists of 8 samples that were generated by printing the real asphalt pore network which was captured using X-ray CT scans (see our previous paper [1] for more details).

Secondly, two groups of computationally-generated samples were generated using the ISA method combined with DE optimisation. A first group (set 2) is a reference group, which consists of 8 samples that were generated to have equivalent air void content, average air void diameter, conductivity and tortuosity as the real asphalt samples (set 1). This set was built to physically validate the model described above as a tool to create asphalt porous materials for computational and physical testing.

A second group of 24 samples (sets 3, 4, 5 and 6) was generated with similar properties to set 2 in terms of air void content, Euler number and tortuosity, but with lower or higher average air void contents than

the reference set. This was done to study the effect of the air void diameter alone on the hydraulic conductivity of porous asphalt.

2.6 3D printed samples fabrication

Figure 4 shows the workflow for the design and manufacturing of samples corresponding to real and computationally-generated pore networks:

1. The pores and asphalt materials (aggregate and bitumen) were differentiated using X-ray CT scans. 3D models of the air voids in asphalt mixture were generated using Avizo 8.1 and ImageJ (more details on this approach can be found in [1]).
2. Cropped volumes of 80 mm x 25 mm x 50 mm were taken from the centre of 3D models.
3. Resin blocks with equivalent air voids to those of asphalt mixture were printed using a Formlabs Form 2 printer with 50 μm resolution, using the commercially-available Formlabs Clear FLGPCL02 proprietary resin [35].
4. The support structure was cut manually from the model and then submerged in isopropanol alcohol for 10 minutes, to make sure that all the resin within the pores had been removed.
5. The samples were polished using super fine 600-grit sandpaper and finished with acrylic spray to enhance samples transparency [36].

The approach taken for computationally-generated samples is similar to the above, except from the fact that the ISA method was used to generate the air voids instead of CT scanning asphalt test samples (see Figure 4).

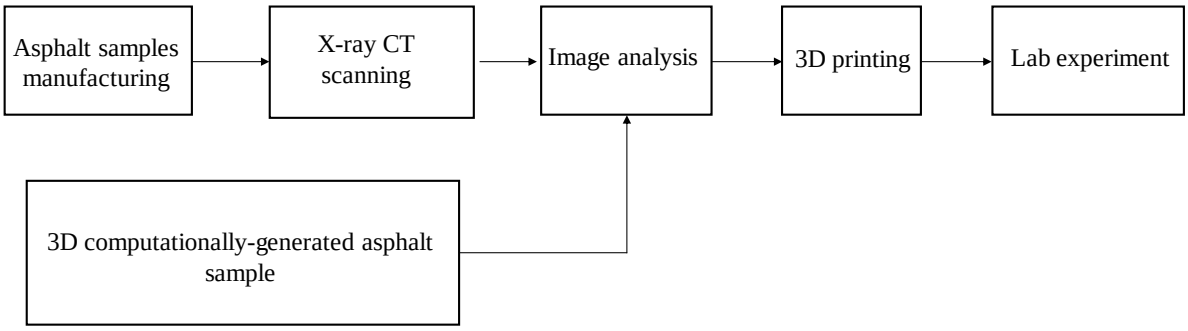

Figure 4: Workflow for fabrication of the test samples for real and computationally-generated 3D printed samples.

2.7 Hydraulic conductivity experimental set up

The hydraulic conductivity tests were carried out at room temperature (20 ^{o}C), following the Florida falling head method [37].

Figure 5 shows the apparatus and experimental setup used to measure the hydraulic conductivity of 3D printed samples:

1. Four acrylic plastic sides were used to build a graduated column with a 30-cm-high rectangular cross section around the asphalt sample or 3D printed resin block with equivalent air voids. Then, the column sides were tightly wrapped using tape and silicone sealant to prevent water leakage during the experiment.
2. The graduated acrylic column was then attached to a plastic plate with a rectangle hole (7cm x 2cm) in its centre to allow the water to flow through the sample.
3. A rubber cylinder was placed in a hollow metal cylinder with a hole in the bottom to allow water movement.
4. Finally, the graduated acrylic column was placed on top of a plastic tube, sealed with silicon and then placed inside the rubber cylinder.

In order to measure the permeability coefficient (k), the time that 100 ml of water required to pass through the test samples was measured. The permeability coefficient (k) was calculated based on Darcy's law [38], as it is explanied in [1].

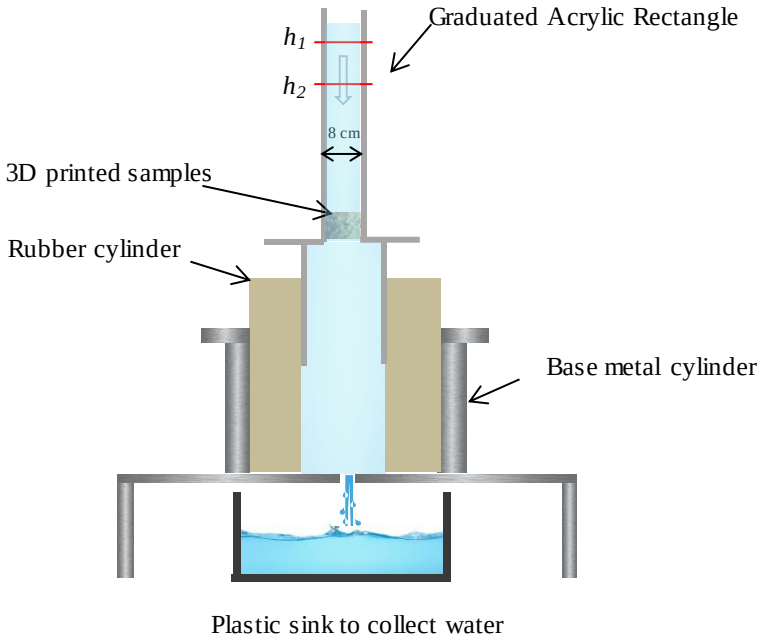

Figure 5: Schematic representation of the hydraulic conductivity test setup (Modified from [1]).

Table 2: Topological constants and hydraulic conductivity of all 3D printed samples studied in this research.

		Sample number	Macroporosity (%)	Average void diameter (mm)	Euler number	Percolation number	Tortuosity	Hydraulic conductivity (cm/s) *10^{-5}
Real 3D printed samples (Set 1)		1	15.6	1.79	-132	0.96	1.48	2024.7
		2	17.9	1.72	-390	0.93	1.34	7866.0
		3	16.1	1.78	-142	0.94	1.37	5307.1
		4	17.8	1.98	-267	0.96	1.22	7883.5
		5	21.6	2.07	-332	0.99	1.18	28237.4
		6	22.6	2.43	-229	1.00	1.13	32654.8
		7	26.3	2.54	-375	1.00	1.11	41614.8
		8	29.8	2.52	-340	0.99	1.10	83348.0
Computationally-generated 3D printed samples (Set 2)		9	15.3	1.69	-255	0.94	1.51	3947.6
		10	15.9	1.78	-141	0.92	1.32	5518.0
		11	18.3	1.94	-317	0.95	1.30	7638.1
		12	19.8	2.00	-248	0.96	1.23	15547.1
		13	21.0	2.20	-408	0.98	1.14	30834.0
		14	23.9	2.30	-457	0.98	1.16	32929.4
		15	25.8	2.53	-475	0.99	1.13	50529.3
		16	31.8	2.71	-576	1.00	1.09	92429.5
Computationally-generated 3D printed with low A_{vd}* (Set 3)		17	14.6	1.44	-294	0.93	2.02	1962.6
		18	15.9	1.54	-367	0.95	1.28	4000.0
		19	18.2	1.59	-343	0.94	1.53	6050.9
		20	19.8	1.74	-256	0.97	1.48	7597.5
		21	21.1	1.87	-416	0.98	1.33	15889.0
		22	24.0	1.94	-459	0.98	1.15	20364.7
		23	25.8	2.23	-488	0.99	1.19	46851.1
		24	30.3	2.43	-594	1.00	1.13	92231.1
Computationally-generated 3D printed with high A_{vd}* (Set 4)		25	15.0	1.99	-209	0.94	1.44	4243.2
		26	15.9	2.06	-161	0.94	1.29	8363.7
		27	18.9	2.23	-241	0.96	1.25	18312.6
		28	20.0	2.36	-215	0.98	1.23	33873.6
		29	21.4	2.56	-235	0.99	1.19	41809.0
		30	23.9	2.64	-301	0.99	1.08	50586.3
		31	26.2	2.85	-224	1.00	1.13	93298.3
		32	31.8	2.98	-284	0.99	1.11	171787.3
Computationally-generated 3D printed with high A_{vd}+ (Set 5)		33	15.8	2.21	-203	0.99	1.25	36135.5
		34	18.5	2.62	-125	0.98	1.45	33584.4
		35	21.5	2.90	-139	0.99	1.39	64083.9
		36	26.9	3.16	-247	0.99	1.09	129225.1
Computationally-generated 3D printed with low A_{vd}+ (Set 6)		37	14.6	1.29	-239	0.88	1.59	784.3
		38	18.3	1.39	-414	0.96	1.48	3217.5
		39	20.5	1.43	-566	0.96	1.38	9232.5
		40	25.9	1.98	-378	0.98	1.36	21065.8
Porous asphalt mixtures (set 7)	Max aggregate size (6 mm)	41	18.6	1.30	-1340	0.96	1.37	-
		42	16.6	1.33	-631	0.95	1.32	-
		43	23.5	1.43	-1648	0.99	1.19	-
		44	28.1	1.56	-2178	1.00	1.13	-
		45	29.7	1.61	-2674	1.00	1.08	-
	Max aggregate size (10 mm)	46	23.1	1.75	-1112	0.99	1.16	-
		47	21.7	1.86	-810	0.98	1.24	-
		48	21.8	1.88	-614	0.99	1.14	-
		49	22.7	1.80	-1133	0.99	1.13	-
		50	31.3	2.02	-1887	1.00	1.07	-
	Max aggregate size (14 mm)	51	13.6	1.95	-37	0.88	1.39	-
		52	15.8	2.21	-140	0.95	1.34	-
		53	20.9	2.59	-254	0.98	1.25	-
		54	21.7	2.68	-361	0.99	1.15	-
		55	28.6	3.03	-499	1.00	1.06	-

* 15% low or high A_{vd} from reference set 2.
\+ 30% low or high A_{vd} from reference set 2.

3 RESULTS AND DISCUSSION

3.1 Comparison between computationally-generated and real 3D printed topological properties of air voids

The topological constants and hydraulic conductivity of the real and computationally-generated 3D printed samples are listed in Table 2 and the Pearson's correlation coefficient for the properties studied are shown in Table 3. In addition, Figure 6 shows the relationship between the hydraulic conductivity of real and computationally-generated 3D printed samples. Table 3 shows that the computationally-generated and real CT scanned samples have a high degree of similarity in the macroporosity, air void diameter, conductivity and tortuosity values, as the Pearson's correlations (r) are 0.93, 0.97, 0.94 and 0.98, respectively. In addition, Figure 6 shows close values of hydraulic conductivity between real and computationally-generated printed samples (R^2=0.84), indicating that they have similar pore space properties. However, it can be seen that computationally-generated samples have slightly higher hydraulic conductivity values. This could be due to higher Euler numbers in the computationally-generated samples, which leads to more paths connecting the top and bottom surfaces of the samples.

Overall, the results show that the ISA method combined with DE can effectively create realistic 3D pore networks similar to those seen in porous asphalt. Moreover, ***Figure*** 7 shows that, visually, the computationally-generated and real pore networks appear similar, too.

Table 3: Pearson's correlation between real and computationally-generated sample parameters studied.

Macroporosity (M), Average void diameter (Avd), Euler number (χ), Tortuosity (T).

	Pearson's *r*
M	0.93
Avd	0.97
χ	0.94
T	0.98

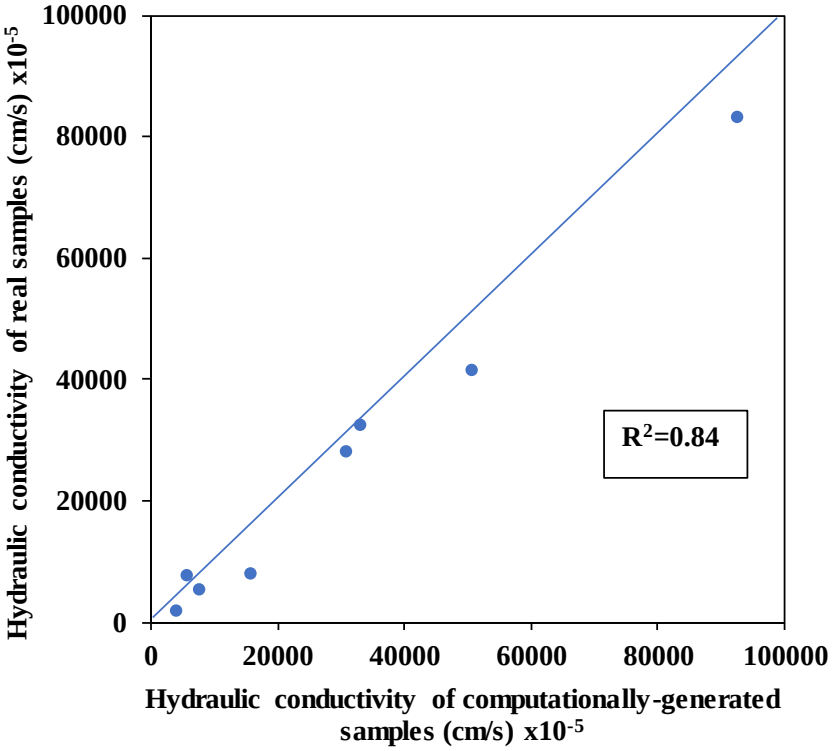

Figure 6: Hydraulic conductivity of real samples versus hydraulic conductivity of computationally-generated samples.

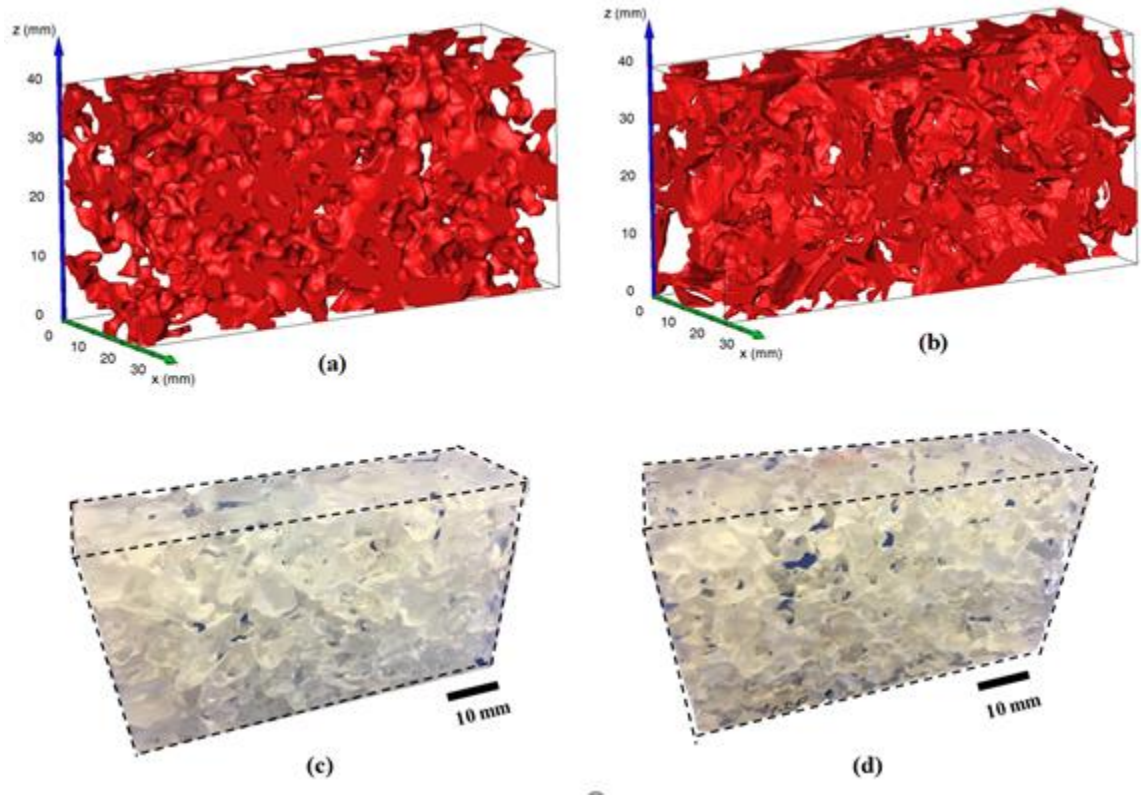

Figure 7: (a) Pore space of the real sample #7, (b) Pore space of the computationally-generated sample #15, (c) 3D printed real sample #7, and (d) 3D printed computationally-generated sample #15.

3.2 Comparison of the pore network structure and shape parameters

Figure 8 shows the pore size distribution for the 3D printed real samples #1, # 4, #7 and the equivalent computationally-generated samples #9, #11, #15. In this paper, we considered pore size instead of average void diameter, as the former parameter captures better the local features of the 3D pore network [39]. It can be seen that the computationally generated samples have a more homogeneous pore size distribution than the real samples. This reflects the fact that the ISA method uses spheres to generate an approximation of the pore space, while real aggregates have more irregular shapes. This difference in pore size distribution can be the reason that computationally-generated samples have higher Euler numbers and hence slightly higher hydraulic conductivity as shown in the section above. However, the differences between real and computationally-generated samples is limited, and the pore size distributions are comparable.

Figure 9 shows the pore circularity, aspect ratio and roundness for the real sample #7 and the computationally-generated sample #15. In Figure 9 (a), it can be observed that the real sample #7 has a slightly higher pore circularity than the computationally-generated sample # 15. Overall, Figure 9 shows that the computationally-generated sample #15 is a close match to the real sample #7 in terms of pore shape size, aspect ratio and roundness of the air voids. This is an indication that the model proposed in this research can successfully create asphalt pore structures with realistic features in terms of the air void shape parameters.

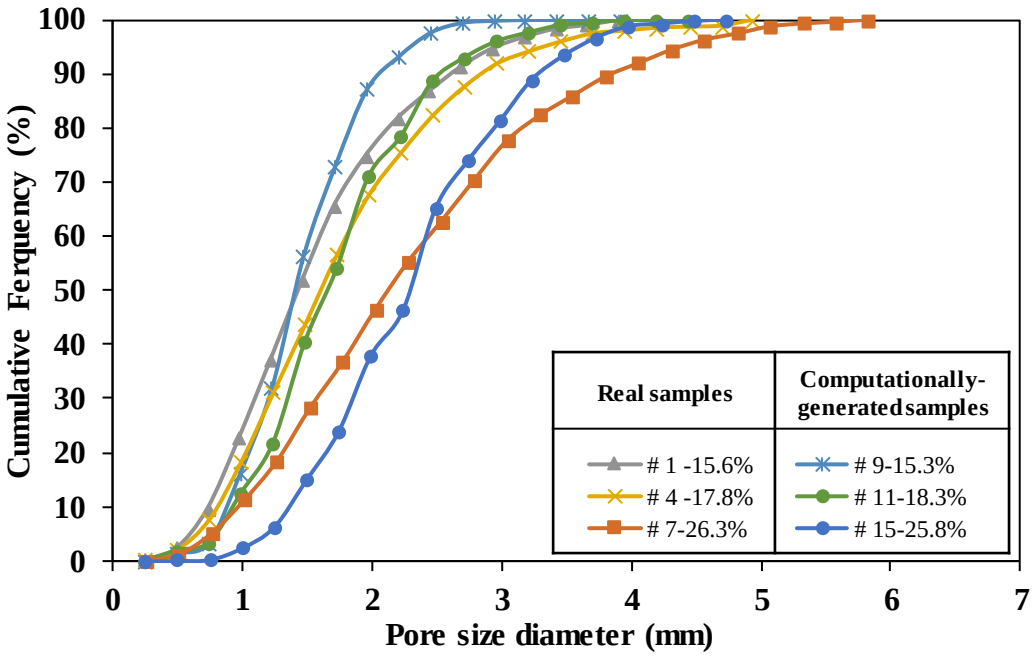

Figure 8: Pore size diameter distributions for the real samples #1, # 4, #7 and the computationally-generated samples #9, #11, #15.

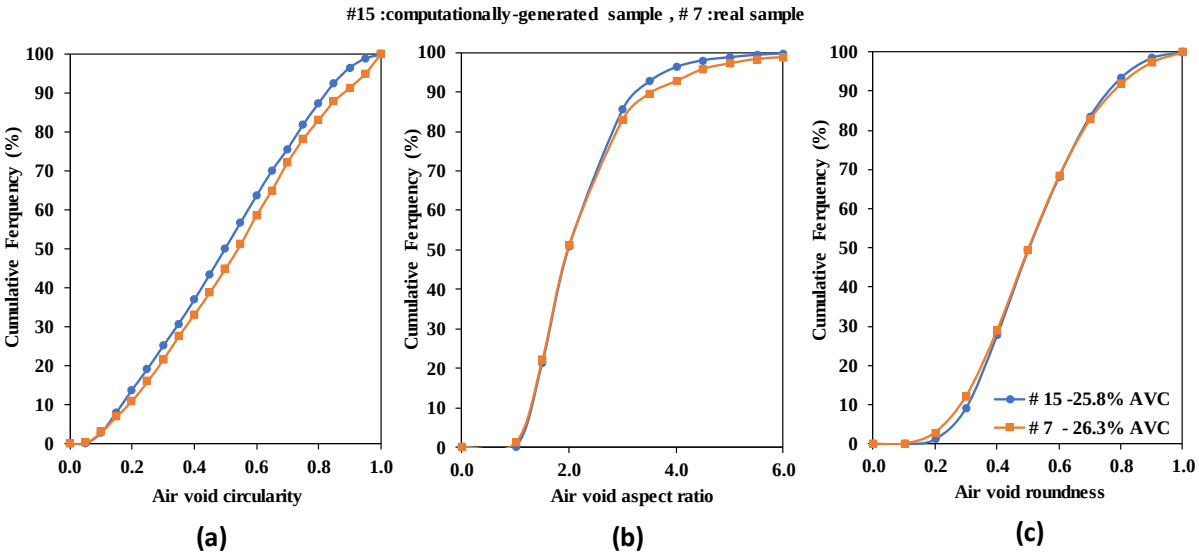

Figure 9: Pore shape parameters of the real samples #7 and computationally-generated sample # 15 (a) Pore shape factor, (b) Aspect ratio and (c) Roundness.

In order to measure the accuracy of the computationally-generated samples, we calculated the autocorrelation function (ACF) [40] using the Radially Averaged Autocorrelation macro, in ImageJ. The ACF characterises the probability of finding two voxels in the 3D space separated with distance (r) that belong to the same phase. These two voxels represent a morphological indicator of an air void structure. Figure 10 shows a comparison between the ACFs for real samples #1, #4, #5, #7 and computationally-generated samples #9, #11, #13, #15. The high similarity between the real and computationally-generated samples curves indicates that the ISA method optimised via DE is a suitable approach to generate asphalt pore macrostructures with realistic features.

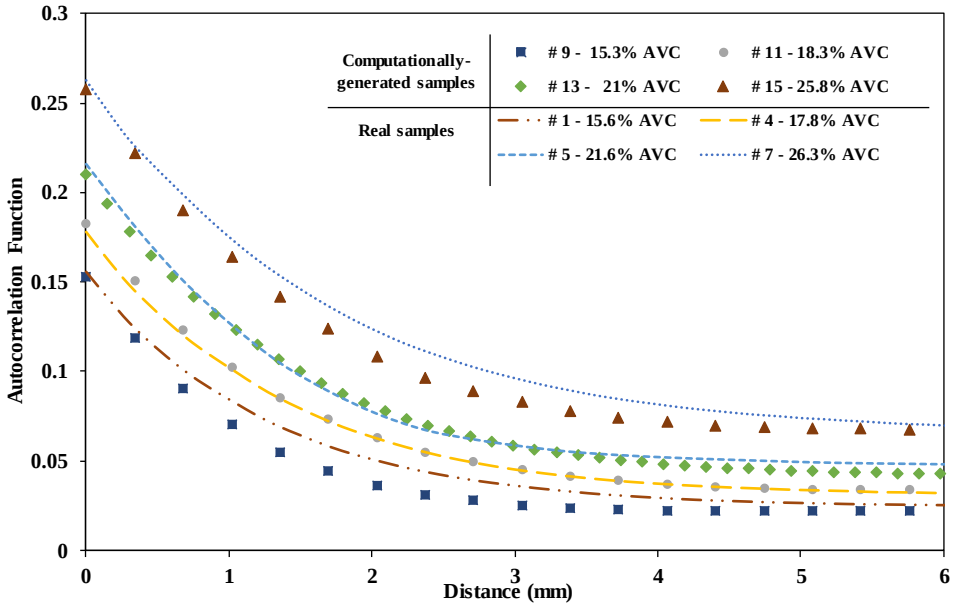

Figure 10: Comparison of the ACF curves of real samples #1, #4, #5, #7 against the computationally-generated sample #9, #11, #13, #15.

3.3 Comparison of the average void diameter for real porous asphalt samples made with different maximum aggregate size and gradation and 3D printed computationally-generated samples.

The topological constant for real porous asphalt samples analyzed using x-ray computed tomography have been represent in Table 2. In addition, Figure 11 shows the effect of maximum aggregate size and aggregate gradation on average void diameter for all real porous asphalt and for computationally-generated asphalt samples. It can be seen that porous asphalt samples with high maximum aggregate size and coarse gradation tend to have a higher average void diameter, while the asphalt samples with lower maximum aggregate size and fine gradation tend to have a lower average void diameter.

Moreover, computationally-generated samples of set 6, i.e. samples generated with low A_{vd}, are visually equivalent to real samples made with 6 mm maximum aggregate size. Furhermore, computationally-generated samples in Set 5, i.e. computationally-generated samples with high A_{vd}, are visually close to porous asphalt sample made with maximum aggregate size of 14 mm. Furthermore, in Figure 11, a whole range of computationally-generated test specimens, from Sets 3 and 4, with intermediate air void diameters, has been represented to demonstrate that most of the samples studied fell in the range between 6mm and 14mm of maximum aggregate size. In the future, by creating an extensive database of X-ray CT data of asphalt with a range of maximum aggregate sizes and aggregate gradations, it will be possible to re-create exactly the air void structure of every test specimen possible.

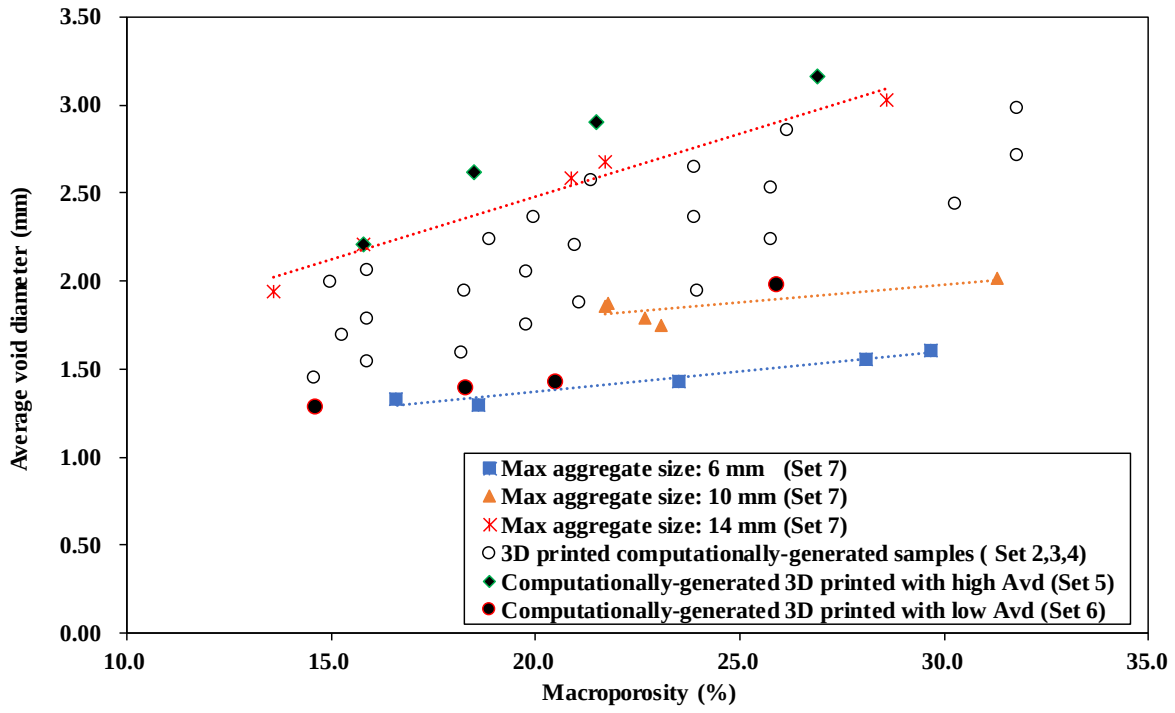

Figure 11: Effect of maximum aggregate size and aggregate gradation on the average void diameter for all real asphalt samples and data for computationally-generated asphalt samples.

3.4 Effect of average void diameter on hydraulic conductivity

The topological constants and hydraulic conductivity for the real and computationally-generated 3D printed samples are represented in Table 2. In addition, Figure 12 shows the effect of the average air void diameter (A_{vd}) on the hydraulic conductivity of computationally-generated 3D printed samples. It can be seen that the hydraulic conductivity increases with the average air void diameter, ranging from $784x10^{-5}$ cm/s at 1.29 mm A_{vd} to 1.71 cm/s at 3 mm A_{vd}.

Furthermore, Figure 12 shows the effect of changing the average air void diameter on the hydraulic conductivity of asphalt mixture when the air void content remains constant. It can be observed that:

- The hydraulic conductivity of samples with air void content from 14.6% to 15.8% ranges between $784x10^{-5}$ cm/s and 0.18 cm/s, when the average void diameter increases from 1.29 mm to 2.21 mm.

- The hydraulic conductivity of samples with air void content from 25.8% to 26.9% ranges between 0.32 cm/s and 1.29 cm/s when the average void diameter increases from 1.98 mm to 3.16 mm.

This suggests that increasing or decreasing the average void diameter significantly affects hydraulic conductivity when the air void content remains constant. Furthermore, it shows that samples with a lower air void content are more sensitive to changes in the average void diameter in terms of their hydraulic conductivity. This is likely to be caused by a smaller connected air pore network. As for example, sample # 33 has percolation number, which represent the volume of the biggest connected air void to the total volume of air void, of 0.99 when A_{vd} is 2.21 mm, while the sample # 37 have percolation number of 0.88 when A_{vd} is 1.29 mm (see Table 2).

Furthermore, in Figure 12, it can be observed that sample #33 with 15.2% air void content can have the same hydraulic conductivity as sample #11 with 18.3% air void content when the average void diameter increases from 1.943 mm to 2.211 mm.

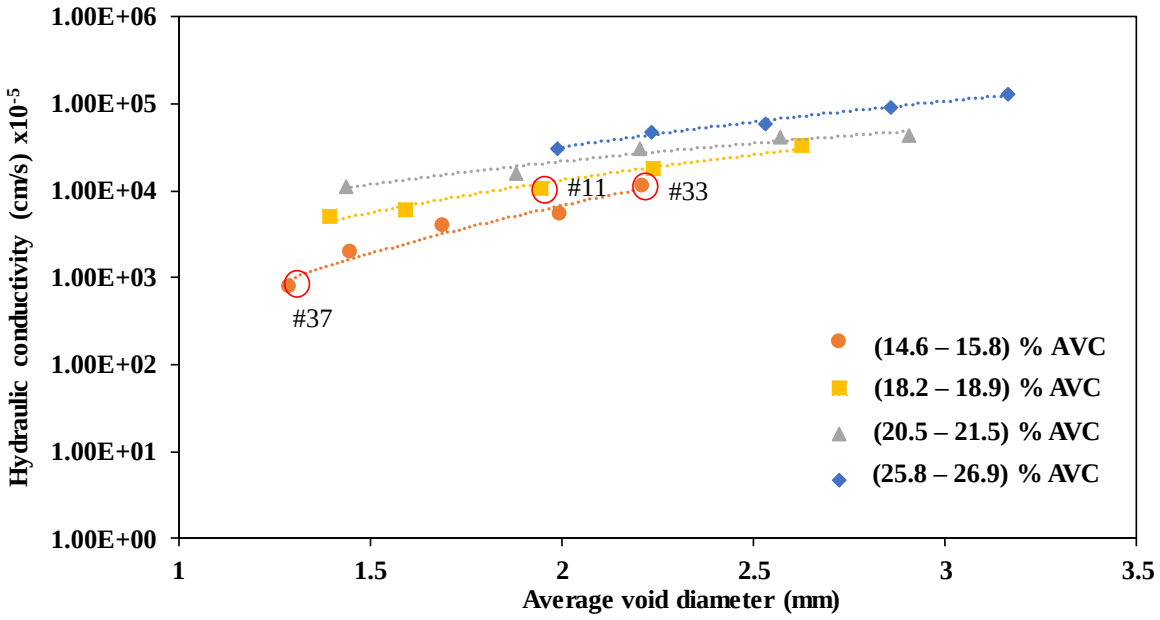

Figure 12: Effect of average void diameter on the hydraulic conductivity for computationally-generated asphalt samples.

3.5 Effect of air void properties on hydraulic conductivity

Figure 13 shows the hydraulic conductivity for all computationally-generated printed samples against several hydraulic conductivities of asphalt mixture, obtained from data in the literature [41-54]. It can be seen that the printed samples built using different average air void diameters, have a range of hydraulic conductivities which matches existing data from the literature.

Moreover, Figure 13 shows that most of the hydraulic conductivity data points from the literature fall between the experimental curves obtained in this study. For example, test samples from Set 6 are equivalent to materials built with maximum aggregate size 6 mm and, test samples from Set 5 are equivalent to materials built with maximum aggregate size 14 mm. This may mean that the dispersion in hydraulic conductivity at constant air void content arises from variations in the average air void diameter, which in the field can happen due to the changing aggregate gradation and maximum aggregate size as shown in section 3.3. Based on this, we could predict the hydraulic conductivity of an asphalt mixture by knowing its air void content [1] and maximum aggregate size.

Finally, in Figure 13, it can also be observed that some samples from the literature fell outside the range measured, especially at air void content lower than approximately 15%. This may be caused by a very low average void diameter, which indicates that these samples have pore networks with few connections, positive Euler number and low percolation number and, posible, small maximum aggregate size (such as a mastic type mixture). Furthermore, the data represented in Figure 13 show that sets 5 and 6, i.e computationally-generated samples equivalent to materials with maximum aggregate size 14mm and

6mm, respectively, correspond to the approximate upper and lower percentile curves of hydraulic conductivity.

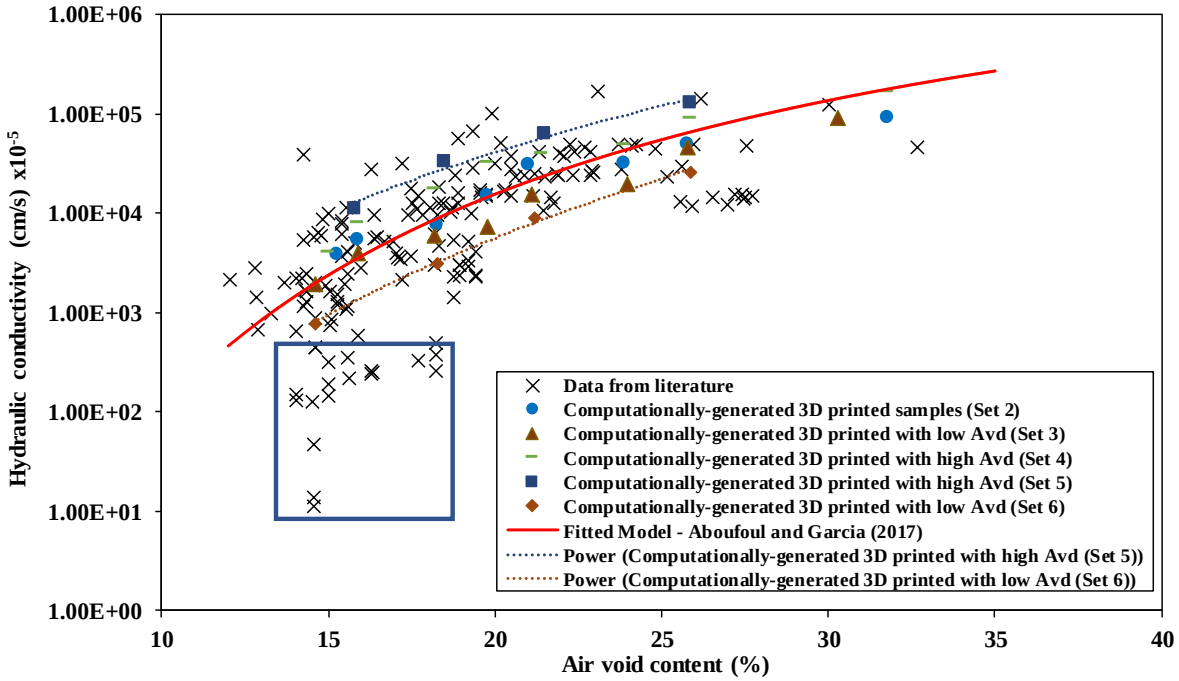

Figure 13: Hydraulic conductivity versus air void content for all samples studied and data from literature [41-54].

4 CONCLUSIONS

In this study, a range of pore space of porous asphalt samples were generated using a virtual air pore generator optimized by differential evolution (DE) algorithm and 3D printed in resin blocks. Moreover, the permeability test was conducted on the 3D samples to understand the effect of pore topology such as average void diameter on the hydraulic conductivity. Based on the research discussed in this paper, the following conclusions can be drawn:

1- The Stacked Intersected Air voids (ISA) method, described in [7, 14, 27], can generate 3D pore networks equivalent to those in asphalt mixtures, in terms of visual, topological, statistical and air void shape properties. This makes possible to precisely investigate water permeability using 3D printing technology rather than using test samples and X-ray CT scans.

2- Differential evolution (DE) algorithms can be used to optimise the ISA method, as the approach uses a set of five input parameters that can be combined to generate a target pore space.

3- When the average air void diameter decreases for the samples with constant air void content, (1) the percolation number decreases, which means that samples have a less connected pore networks; and (2) the hydraulic conductivity decreases.

4- The average air void diameter has significant influence on the hydraulic conductivity of asphalt mixture with equivalent air void content range. Increasing the average void diameter tends to decrease the hydraulic conductivity of the sample, as the number of paths from the sample surface to its bottom decreases. However, the few paths have a higher diameter which reflects the higher hydraulic conductivity.

5- Based on all the information presented in this paper, we can predict the range of average void diameter, and so we can find the aggregate gradation and maximum aggregate size based on hydraulic conductivity and air void content for porous asphalt materials in the range of porosity studied in this study.

6- Future research should focus on the effects of topological properties such as connectivity and tortuosity on hydraulic conductivity of porous asphalt materials. Furthermore, the effects of aggregate gradation, binder content, compaction level, type of aggregate and maximum aggregate size on the topological parameters and hydraulic conductivity remains to be investigated.

ACKNOWLEDGEMENTS

Mustafa Aboufoul would want to acknowledge his PhD sponsorship by the University of Nottingham through the Scholarship for International Excellence from the Faculty of Engineering.

REFERENCES

[1] M. Aboufoul, A. Garcia, Factors affecting hydraulic conductivity of asphalt mixture, Materials and Structures, 50 (2017) 116.
[2] M. Scholz, P. Grabowiecki, Review of permeable pavement systems, Building and Environment, 42 (2007) 3830-3836.
[3] M. Aboufoul, A. Garcia, Influence of air voids characteristics on the hydraulic conductivity of asphalt mixture, Road Materials and Pavement Design, (2017) 1-11.
[4] E. Kassem, E. Masad, R. Lytton, R. Bulut, Measurements of the moisture diffusion coefficient of asphalt mixtures and its relationship to mixture composition, International Journal of Pavement Engineering, 10 (2009) 389-399.
[5] S. Katuwal, P. Moldrup, M. Lamandé, M. Tuller, L.W. De Jonge, Effects of CT number derived matrix density on preferential flow and transport in a macroporous agricultural soil, Vadose Zone Journal, 14 (2015).
[6] S. Katuwal, T. Norgaard, P. Moldrup, M. Lamandé, D. Wildenschild, L.W. de Jonge, Linking air and water transport in intact soils to macropore characteristics inferred from X-ray computed tomography, Geoderma, 237 (2015) 9-20.
[7] A. Chiarelli, A. Dawson, A. Garcia, Stochastic generation of virtual air pores in granular materials, Granular Matter, 17 (2015) 617-627.
[8] J. Chen, B. Huang, F. Chen, X. Shu, Application of discrete element method to Superpave gyratory compaction, Road Materials and Pavement Design, 13 (2012) 480-500.
[9] H. Feng, M. Pettinari, B. Hofko, H. Stang, Study of the internal mechanical response of an asphalt mixture by 3-D discrete element modeling, Construction and Building materials, 77 (2015) 187-196.
[10] H. Okabe, M.J. Blunt, Prediction of permeability for porous media reconstructed using multiple-point statistics, Physical Review E, 70 (2004) 066135.
[11] J.D. Hyman, P.K. Smolarkiewicz, C.L. Winter, Heterogeneities of flow in stochastically generated porous media, Physical Review E, 86 (2012) 056701.
[12] M. Siena, M. Riva, J. Hyman, C.L. Winter, A. Guadagnini, Relationship between pore size and velocity probability distributions in stochastically generated porous media, Physical Review E, 89 (2014) 013018.
[13] I. Schenker, F.T. Filser, L.J. Gauckler, Stochastic generation of particle structures with controlled degree of heterogeneity, Granular matter, 12 (2010) 437-446.
[14] A. Chiarelli, A. Dawson, A. Garcia, Generation of virtual asphalt mixture porosity for computational modelling, Powder Technology, 275 (2015) 351-360.
[15] D. Pham, D. Karaboga, Intelligent optimisation techniques: genetic algorithms, tabu search, simulated annealing and neural networks, Springer Science & Business Media2012.
[16] R. Storn, K. Price, Differential evolution–a simple and efficient heuristic for global optimization over continuous spaces, Journal of global optimization, 11 (1997) 341-359.
[17] E. MacDonald, R. Wicker, Multiprocess 3D printing for increasing component functionality, Science, 353 (2016) aaf2093.
[18] R. Goodridge, C. Tuck, R. Hague, Laser sintering of polyamides and other polymers, Progress in Materials Science, 57 (2012) 229-267.
[19] E. Saleh, F. Zhang, Y. He, J. Vaithilingam, J.L. Fernandez, R. Wildman, I. Ashcroft, R. Hague, P. Dickens, C. Tuck, 3D inkjet printing of electronics using UV conversion, Advanced Materials Technologies, 2 (2017).
[20] K. Osei-Bonsu, P. Grassia, N. Shokri, Relationship between bulk foam stability, surfactant formulation and oil displacement efficiency in porous media, Fuel, 203 (2017) 403-410.
[21] D. Head, T. Vanorio, Effects of changes in rock microstructures on permeability: 3-D printing investigation, Geophysical Research Letters, 43 (2016) 7494-7502.

[22] S. Ishutov, F.J. Hasiuk, D. Jobe, S. Agar, Using Resin-Based 3D Printing to Build Geometrically Accurate Proxies of Porous Sedimentary Rocks, Groundwater, (2017).
[23] B.M. BS EN 12697-31, Test Methods for Hot Mix Asphalt: Specimen prepared by gyratory compactor, British Standard Institute (BSI), (2007).
[24] J. Wang, A. Goyanes, S. Gaisford, A.W. Basit, Stereolithographic (SLA) 3D printing of oral modified-release dosage forms, International journal of pharmaceutics, 503 (2016) 207-212.
[25] M. Bacher, 3D-printing of undisturbed soil imaged by X-ray, (2013).
[26] N. Ahmad, Asphalt mixture moisture sensitivity evaluation using surface energy parameters, University of Nottingham, 2011.
[27] A. Chiarelli, A. Dawson, A. Garcia, Generation Of 3D Soil/Asphalt Porosity Patterns For Numerical Modelling, From Fundamentals to Applications in Geotechnics. Proceedings of the 15th Pan-American Conference on Soil Mechanics and Geotechnical Engineering, 15-18 November 2015, Buenos Aires, Argentina, IOS Press, 2015, pp. 1089 - 1096.
[28] A. Rabbani, S. Jamshidi, S. Salehi, An automated simple algorithm for realistic pore network extraction from micro-tomography images, Journal of Petroleum Science and Engineering, 123 (2014) 164-171.
[29] D. Legland, K. Kiêu, M.-F. Devaux, Computation of Minkowski measures on 2D and 3D binary images, Image Analysis & Stereology, 26 (2011) 83-92.
[30] R.I. Al-Raoush, I.T. Madhoun, TORT3D: A MATLAB code to compute geometric tortuosity from 3D images of unconsolidated porous media, Powder Technology, 320 (2017) 99-107.
[31] D. Gómez-Lorente, I. Triguero, C. Gil, A.E. Estrella, Evolutionary algorithms for the design of grid-connected PV-systems, Expert Systems with Applications, 39 (2012) 8086-8094.
[32] V. Arunachalam, Optimization using differential evolution, (2008).
[33] S. Das, S.S. Mullick, P.N. Suganthan, Recent advances in differential evolution–an updated survey, Swarm and Evolutionary Computation, 27 (2016) 1-30.
[34] K. Price, R.M. Storn, J.A. Lampinen, Differential evolution: a practical approach to global optimization, Springer Science & Business Media2006.
[35] O. Okafor, A. Weilhard, J.A. Fernandes, E. Karjalainen, R. Goodridge, V. Sans, Advanced reactor engineering with 3D printing for the continuous-flow synthesis of silver nanoparticles, Reaction Chemistry & Engineering, 2 (2017) 129-136.
[36] H. Yoon, M.J. Martinez, T. Dewers, 3D Printing and Digital Rock Physics for Geoscience Applications, Sandia National Lab.(SNL-NM), Albuquerque, NM (United States), 2016.
[37] D. Florida, Florida method of test for measurement of water permeability of compacted asphalt paving mixtures, FM5-565, Dept. of Transportation, Tallahassee, FL, (2004).
[38] FM5-565, Florida Standard Test Method FM5-565-Measurement of Water Permeability of Compacted Asphalt Paving Mixtures, Florida Department of Transportation, Tallahassee, (1997).
[39] Y. Wu, C. Lin, L. Ren, W. Yan, S. An, B. Chen, Y. Wang, X. Zhang, C. You, Y. Zhang, Reconstruction of 3D porous media using multiple-point statistics based on a 3D training image, Journal of Natural Gas Science and Engineering, (2018).
[40] Y. Li, X. He, Q. Teng, J. Feng, X. Wu, Markov prior-based block-matching algorithm for superdimension reconstruction of porous media, Physical Review E, 97 (2018) 043306.
[41] B. Birgisson, R. Roque, G.C. Page, Evaluation of water damage using hot mix asphalt fracture mechanics (with discussion), Journal of the association of asphalt paving technologists, 72 (2003).
[42] R.J. Charbeneau, J.B. Klenzendorf, M.E. Barrett, Methodology for determining laboratory and in situ hydraulic conductivity of asphalt permeable friction course, Journal of Hydraulic Engineering, 137 (2010) 15-22.
[43] L.A. Cooley, B.D. Prowell, E.R. Brown, Issues pertaining to the permeability characteristics of coarse-graded Superpave mixes, ASPHALT PAVING TECHNOLOGY, 71 (2002) 1-29.
[44] A. Gogula, M. Hossain, S.A. Romanoschi, A Study of Factors Affecting the Permeability of Superpave Mixtures in Kansas, Kansas Department of Transportation, (2004).
[45] K. Kanitpong, H. Bahia, C. Benson, X. Wang, Measuring and predicting hydraulic conductivity (permeability) of compacted asphalt mixtures in the laboratory, 82nd Annual Meeting of the Transportation Research Board, Washington, DC, 2003.
[46] M.E. Kutay, A.H. Aydilek, E. Masad, T. Harman, Computational and experimental evaluation of hydraulic conductivity anisotropy in hot-mix asphalt, International Journal of Pavement Engineering, 8 (2007) 29-43.

[47] R.B. Mallick, L.A. Cooley, M.R. Teto, R.L. Bradbury, D. Peabody, An evaluation of factors affecting permeability of Superpave designed pavements, National Center for Asphalt Technology, Report, (2003) 03-02.
[48] B.J. Putman, Evaluation of Open-Graded Friction Courses: Construction, Maintenance, and Performance, Rep. No. FHWA-SC-12-04, Clemson Univ., South Carolina Dept. of Transportation, (2012).
[49] M.M. Sprinkel, A.K. Apeagyei, Evaluation of the Installation and Initial Condition of Rosphalt Overlays on Bridge Decks, 2013.
[50] Y. Jang, D. Kim, S. Mun, B. Jang, Proposal for the Estimation of the Hydraulic Conductivity of Porous Asphalt Concrete Pavement using Regression Analysis, International Journal of Highway Engineering, 15 (2013) 45-52.
[51] J. Norambuena-Contreras, E.A. Izquierdo, D. Castro-Fresno, M.N. Partl, Á. Garcia, A New Model on the Hydraulic Conductivity of Asphalt Mixtures, International Journal of Pavement Research and Technology, 6 (2013) 488.
[52] P. Romero, Laboratory evaluation of the PQI model 300, Report to FHWA, (2000).
[53] A. Setiawan, Design and Properties of Hot Mixture Porous Asphalt for Semi-Flexible Pavement Applications, Media Teknik Sipil, 5 (2009) 41-46.
[54] M.M. Sprinkel, A.K. Apeagyei, Evaluation of the Installation and Initial Condition of Thermoplastic Polymer-modifed Asphalt Overlays on Bridge Decks, Transportation Research Board 93rd Annual Meeting, 2014.

Appendix:

Table 4: Aggregate grading and binder content used to produce porous asphalt mixtures.

Max aggregate size	6 mm					10 mm					14 mm				
Target porosity	13%	17%	21%	26%	29%	13%	17%	21%	26%	29%	13%	17%	21%	26%	29%
sieve size (mm)	Cumulative aggregate weight % passing														
63.000	100	100	100	100	100	100	100	100	100	100	100	100	100	100	100
40.000	100	100	100	100	100	100	100	100	100	100	100	100	100	100	100
31.500	100	100	100	100	100	100	100	100	100	100	100	100	100	100	100
20.000	100	100	100	100	100	100	100	100	100	100	100	100	100	100	100
16.000	100	100	100	100	100	100	100	100	100	100	100	100	100	100	100
14.000	100	100	100	100	100	100	100	100	100	100	97	96	96	95	95
10.000	100	100	100	100	100	94	94	94	93	93	55	51	44	38	34
8.000	100	100	100	100	100	72	70	67	65	64	37	33	25	19	14
6.300	97	97	97	96	96	42	39	34	30	27	29	25	19	16	11
4.000	49	45	41	36	31	22	19	15	12	8	22	19	14	12	7
2.800	35	29	24	19	12	18	15	12	10	6	20	17	12	11	6
2.000	29	24	20	15	9	16	13	11	8	5	17	15	11	9	5
1.000	21	18	14	11	7	12	10	8	6	4	13	11	8	7	4
0.500	16	13	11	8	5	8	7	6	5	3	9	8	6	5	3
0.250	12	10	8	7	4	7	6	5	4	2	7	6	5	4	3
0.125	9	8	7	5	4	5	4	4	3	2	6	5	4	3	2
0.063	7	6	5	4	3	4	4	3	2	2	4	4	3	3	2
Binder content (%)	6	5.7	5.5	5.3	5	5.5	5.2	4.8	4.3	4.2	5	4.7	4.5	4.3	4